

## Multiscale molecular simulations of the morphological evolution of small-molecule organic solar cells during the vacuum codeposition process

Ping-Han Tang,<sup>1</sup> Ping-Hong Chen,<sup>2</sup> Fang-Cheng Li<sup>1</sup>, Chien-Hao Lu,<sup>1</sup> Ching-I Huang,<sup>2,\*</sup> and Chun-Wei Pao<sup>1,†</sup>

<sup>1</sup>Research Center for Applied Sciences, Academia Sinica, Taipei 11529, Taiwan, Republic of China

<sup>2</sup>Institute of Polymer Science and Engineering, National Taiwan University, Taipei 10617, Taiwan, Republic of China



(Received 4 March 2020; accepted 7 August 2020; published 8 September 2020)

The mesoscale morphologies of organic small molecule films fabricated via vacuum deposition processes are critical to the performance of small-molecule solar cells and organic light-emitting diodes. In the present study, the morphological evolution of the active layer of DPDCPB:C<sub>70</sub> small-molecule solar cells during vacuum codeposition processes was revealed by a series of GPU-accelerated coarse-grained molecular-dynamics simulations. The C<sub>70</sub> and DPDCPB molecules were coarsened into ellipsoids and bonded ellipsoids, respectively. The interactions between ellipsoids were described by the Gay-Berne formulation and were parametrized to reproduce potential energy surfaces from all-atom atomistic simulations using a genetic algorithm. Due to the significantly reduced overall degrees of freedom, this coarse-grained scheme allowed us to simulate the vacuum codeposition processes and monitor the morphological evolution of systems with system length scales compatible with those of the experiments (~30 nm). Our simulations indicate that the film morphologies are closely correlated with the DPDCPB:C<sub>70</sub> blending ratio. High C<sub>70</sub> concentration leads to a rough film surface, which is in accordance with experimental observations and can be attributed to the strong self-aggregation behavior of C<sub>70</sub> molecules. The morphological property analysis indicates that the rough film surface has an almost negligible impact on the DPDCPB/C<sub>70</sub> domain percolations, and the device with the optimal deposition ratio should give the most balanced hole/electron transfer in respective DPDCPB/C<sub>70</sub> domains. The present study demonstrates that by using the ellipsoid-based coarse-grained model, it is possible to study the morphological evolution of small-molecule organic thin film during vacuum deposition processes with molecular scale details, which can provide valuable insights for experimental teams to further optimize device fabrication protocols for the next generation of organic optoelectronic devices.

DOI: [10.1103/PhysRevMaterials.4.095601](https://doi.org/10.1103/PhysRevMaterials.4.095601)

### I. INTRODUCTION

Vacuum deposition processes have been extensively employed for the fabrication of organic electronic devices such as high-performance small-molecule organic solar cells—one of the most promising renewable energy sources—and organic light-emitting diodes [1–10]. These organic electronic devices often comprise multiple constituent molecules; for example, the active layers of small-molecule organic solar cells comprise electron donor and electron acceptor molecules. During the deposition of small-molecule organic solar cells, small molecular donors and acceptors evaporate from crucibles and deposit onto substrates in the deposition chamber. Subsequent surface interdiffusion processes of donor/acceptor molecules promote phase separation between donor and acceptor molecules, leading to the formation of the bulk heterojunction layer [11,12]. The mesoscale morphologies of the bulk heterojunction layer are critical to device performance [13,14] and are sensitive to device fabrication parameters such as the donor/acceptor blending ratio [7]; hence, the revelation of the process-structure correlation is crucial to

help experimental teams fine-tune their fabrication protocols to further optimize device performance [14].

Experimental characterizations offer the most direct measure to elucidate the correlations between morphologies and fabrication protocols [14]. However, for small-molecule organic solar cells, in contrast to their polymer counterparts, there exists a lack of three-dimensional morphological data obtained directly from experiments. Therefore, computer simulations have become a potential tool to reveal the morphological evolution of the bulk heterojunction layers of small-molecule solar cells during vacuum deposition processes [15]. The system size of interest of small-molecule solar cells is on the order of 50–100 nm, well beyond the reach of *ab initio* simulations and still considered computationally intensive for classical molecular-dynamics (MD) simulations. Coarse-grained molecular-dynamics (CGMD) simulations have been extensively employed to investigate the mesoscale morphologies of polymer solar cells [15,16]. The morphology of SMDPPEH:PCBM small-molecule solar cells formed from solution processing has been investigated by using an ellipsoid-based CG model [16]. In this study, we extended the simple ellipsoid CG model of SMDPPEH:PCBM blends to bonded ellipsoids to simulate the vacuum codeposition process of 2- $\{[7-(4-N,N$ -diphenylaminophenyl-1-yl)-2,1,3-benzothiadiazol-4-yl]methylene\} malononitrile

\*chingih@ntu.edu.tw

†cwpao@gate.sinica.edu.tw

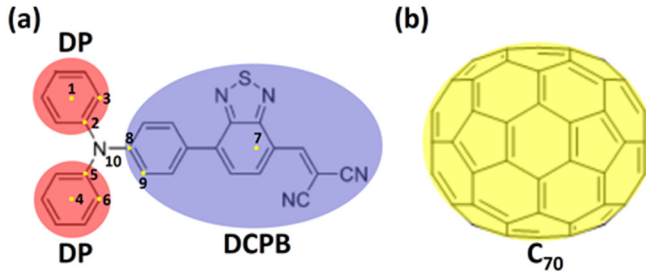


FIG. 1. The CG scheme employed in the present study: (a) DPDCPB molecule and (b)  $C_{70}$  molecule.

(DPDCPB): $C_{70}$  small-molecule blends, which has shown great potential for applications in high-performance organic photovoltaic devices for both single and tandem junction device architectures [17]. In this study, the interactions between ellipsoid CG particles were described by the Gay-Berne formulation and were parametrized to reproduce the potential energy surfaces from respective all-atom atomistic simulations, whereas the intramolecular force fields (for DPDCPB molecules) were parametrized to reproduce the distribution of CG intramolecular degrees of freedom, namely the CG bond length and angles, from respective all-atom atomistic simulations. The significant reduction in the overall system degrees of freedom allowed us to perform large-scale CGMD simulation of vacuum codeposition processes to examine the three-dimensional morphologies of the bulk heterojunction layers of different DPDCPB: $C_{70}$  blending ratios and to directly compare the surface morphologies with atomic force microscopy (AFM) measurements from experiments [17]. Our CGMD simulations indicate that the DPDCPB: $C_{70}$  film roughness and film qualities are closely correlated with the deposition ratio. Increasing the concentration of  $C_{70}$  leads to a rough film surface and poor film quality, which is consistent with experimental observation from AFM [17]. Subsequent analysis reveals that the strong attractive interaction between  $C_{70}$  molecules is the primary factor leading to the formation of  $C_{70}$  aggregates, which serve as the skeleton of rugged film surface structures. Hence, the present study demonstrates that the bonded ellipsoid CG model can be used to perform large-scale CGMD simulation of vacuum deposition processes of small molecules with system sizes compatible with those of experiments, thereby providing insights into the morphology and film microstructure evolution during the fabrication of small-molecule organic electronic devices such as solar cells and light-emitting diodes.

## II. SIMULATION METHODOLOGIES

The molecular structures of DPDCPB and  $C_{70}$  as well as the CG scheme employed in the present study are depicted in Figs. 1(a) and 1(b), respectively. The DPDCPB molecule was divided into three bonded ellipsoids (one DCPB bead and two DP beads), whereas the  $C_{70}$  molecule was coarse-grained into one single ellipsoid bead. Note that in the DPDCPB molecule, in addition to ellipsoids representing DP and DCPB CG beads [indexed as beads 1, 4, and 7 in Fig. 1(a)], additional virtual atoms (atoms 2, 3, 5, 6, 8, and 9) were embedded into ellipsoids to serve as the anchor points of CG bonds to

account for intramolecular CG degrees of freedom, namely CG bonds, angles, and dihedrals. The CG force fields were obtained based on energies and atomistic trajectories from all-atom atomistic simulations of smaller systems of interest. The intermolecular interactions between ellipsoids were parametrized into the Gay-Berne formulation, which is essentially an orientation-dependent Lennard-Jones potential [18]. The intramolecular CG force fields were divided into contributions from intramolecular CG degrees of freedom, namely CG bonds, angles, and dihedrals, and they were parametrized into respective analytic formulas [19–21].

In the present study, the intermolecular interactions between ellipsoids were described by the Gay-Berne potential [18,22–25]. The Gay-Berne potential can be expressed as the following:

$$U(\mathbf{A}_1, \mathbf{A}_2, r_{12}) = U_r(\mathbf{A}_1, \mathbf{A}_2, r_{12}, \gamma) \eta_{12}(\mathbf{A}_1, \mathbf{A}_2, \nu) \times \chi_{12}(\mathbf{A}_1, \mathbf{A}_2, r_{12}, \mu), \quad (1)$$

where  $\mathbf{A}_1$ ,  $\mathbf{A}_2$ , and  $r_{12}$  are the transformation matrices of the two ellipsoids and the respective center-to-center separation between them.  $U_r$  controls the shifted distance-dependent Lennard-Jones interaction, based on the distance of closest approach between two ellipsoids  $h_{12}$ , which can be expressed in the following form:

$$U_r = 4\varepsilon(\rho^{12} - \rho^6) \quad (2)$$

with

$$\rho = \frac{\sigma}{h_{12} - \gamma\sigma}, \quad (3)$$

where  $\varepsilon$  and  $\sigma$  are the well depth and radius of the shifted LJ potential, respectively, whereas  $\gamma$  is a user-defined shifted parameter.  $h_{12}$  is the shortest distance between two ellipsoids, and it can be approximated by the formula [24]

$$h_{12} = r_{12} - \left[ \frac{1}{2} \hat{\mathbf{r}}_{12}^T \mathbf{G}_{12}^{-1} \hat{\mathbf{r}}_{12} \right]^{-\frac{1}{2}}, \quad (4)$$

where  $\hat{\mathbf{r}}_{12}$  is the center-to-center unit vector pointing from ellipsoid 2 to ellipsoid 1.  $\mathbf{G}_{12}$  can be expressed as

$$\mathbf{G}_{12} = \mathbf{A}_1^T \mathbf{S}_1^2 \mathbf{A}_1 + \mathbf{A}_2^T \mathbf{S}_2^2 \mathbf{A}_2, \quad (5)$$

where  $\mathbf{S}_i = \text{diag}(a_i, b_i, c_i)$  is the shape matrix of the  $i$ th ellipsoid, with  $a_i$ ,  $b_i$ , and  $c_i$  being the semiaxes of the ellipsoid. The two terms  $\eta_{12}$  and  $\chi_{12}$  in Eq. (1) are orientation-dependent energy terms.  $\eta_{12}$  can be expressed as

$$\eta_{12} = \left[ \frac{2s_1 s_2}{\det(\mathbf{G}_{12})} \right]^{v/2}, \quad (6)$$

where  $s_i = (a_i b_i + c_i c_i)(a_i b_i)^{1/2}$ , and

$$\chi_{12} = \left[ 2 \hat{\mathbf{r}}_{12}^T \mathbf{B}_{12}^{-1} \hat{\mathbf{r}}_{12} \right]^\mu, \quad (7)$$

where  $\mathbf{B}_{12}$  can be expressed as

$$\mathbf{B}_{12} = \mathbf{A}_1^T \mathbf{E}_1 \mathbf{A}_1 + \mathbf{A}_2^T \mathbf{E}_2 \mathbf{A}_2. \quad (8)$$

The  $\mathbf{E}_i$  in Eq. (8) is the diagonal matrix defined by the formula  $\mathbf{E}_i = \text{diag}(\varepsilon_{ia}^{-1}, \varepsilon_{ib}^{-1}, \varepsilon_{ic}^{-1})$ ; here,  $\varepsilon_{ia}$ ,  $\varepsilon_{ib}$ , and  $\varepsilon_{ic}$  are dimensionless quantities of the relative potential energy well

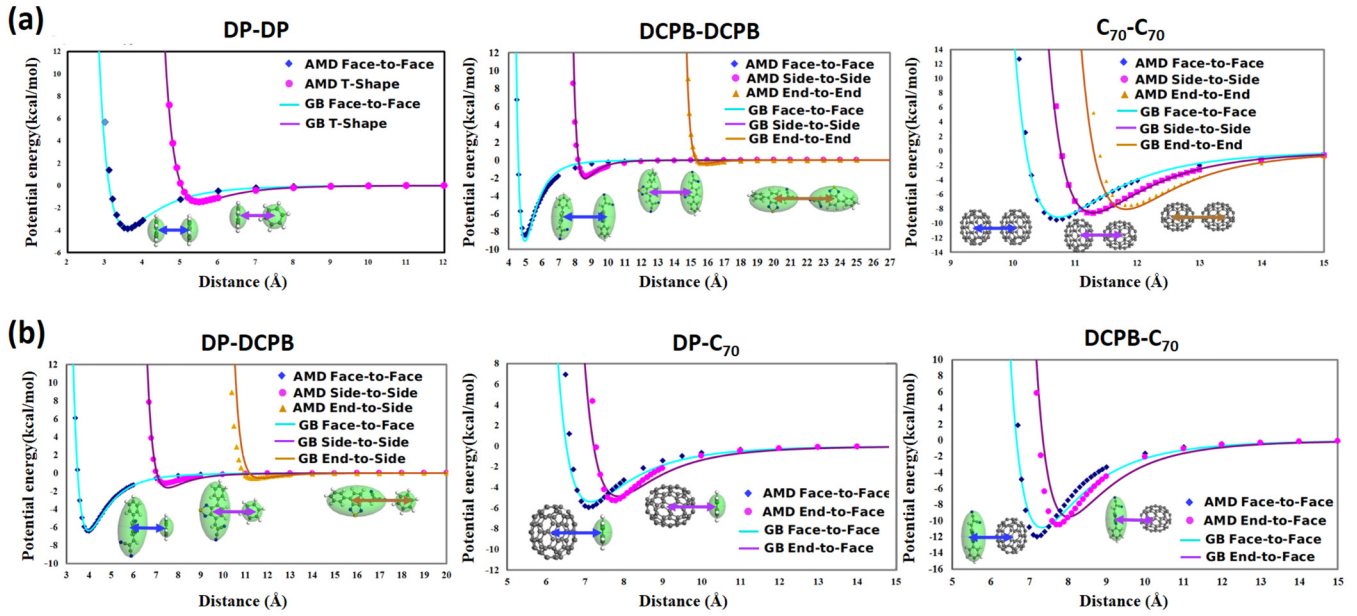


FIG. 2. Pairwise potential energy surfaces from the all-atom atomistic calculations (symbols) and from the parametrized Gay-Berne potentials (lines) of (a) pairs of the same species and (b) pairs of different species.

depths for the face-to-face, side-to-side, and end-to-end stackings of two ellipsoids [24].

The Gay-Berne potential for intermolecular interactions between DPDCPB and  $C_{70}$  molecules was parametrized to reproduce the pairwise potential energy surfaces (PESs) between CG particles in their respective all-atom representations. A set of PESs from all-atom atomistic simulations of CG ellipsoids (namely, DCPB, DP, and  $C_{70}$ ) was computed as a function of separation. In the present study, the Dreiding force field [26] was employed for all-atom atomistic calculation of PESs. Note that a variety of stackings, namely face-to-face, side-to-side, or edge-to-edge, were also considered; see Fig. 2. The Gay-Berne potential parameter set  $\{\rho_n\}$  was obtained by minimizing the penalty function  $f$ ,

$$f(\{\rho_n\}) = \frac{1}{N} \sum_{i=1}^N [U_i^{\text{AMD}}(r) - U_i^{\text{GB}}(r, \{\rho_n\})]^2, \quad (9)$$

where  $N$  is the total number of PESs considered (Fig. 2), and  $U_i^{\text{AMD}}$  and  $U_i^{\text{GB}}$  are PESs computed from all-atom atomistic simulations and from Gay-Berne potentials with the parameter set  $\{\rho_n\}$ , respectively. The penalty function was minimized by using the covariant-matrix-adaptation-evolution-strategy (CMAES) algorithm—one of the variants of the genetic algorithm—to search for the global minimum of parameter space [27–34]. The PES curves from both all-atom atomistic calculations and optimized Gay-Berne parameters are displayed in Fig. 2. From Fig. 2, it is evident that PESs derived from the optimized Gay-Berne parameters exhibit very good agreement with those from all-atom atomistic calculations. The optimized Gay-Berne parameter sets were compiled in Table S1 in the Supplemental Material [35]. Furthermore, it is worth noting that the potential energy well depths of  $C_{70}$ - $C_{70}$  and DCPB- $C_{70}$  are noticeably deeper than those of other pairs of interaction, suggesting the enhancement of aggregation of  $C_{70}$  molecules and the possibility of formation of DCPB- $C_{70}$

core-shell structures as the concentration of  $C_{70}$  molecules increases. Note that the cutoff distance for the Gay-Berne potential was set to 30 Å in the present study.

As depicted in Fig. 1, the CG representation of the DPDCPB molecule comprises three ellipsoids connected by bonds centered at the N atom [atom 10 in Fig. 1(a)]. To parametrize the intramolecular CG force field of the DPDCPB molecule, we performed all-atom atomistic molecular-dynamics simulations of DPDCPB molecules, and we computed the probability distributions of the CG intramolecular degrees of freedom, namely bonds, angles, and dihedrals. Similar to earlier CGMD studies of polymer solar cells, the intramolecular CG force fields were constructed by using Boltzmann inversion [15]. The potential functions were then parametrized into analytic forms. Harmonic potentials were employed for both CG bond and angle interactions, namely

$$E = K_r(r - r_0)^2 \text{ for bonds}, \quad (10)$$

$$E = K_\theta(\theta - \theta_0)^2 \text{ for angles}. \quad (11)$$

The dihedral degrees of freedom were parametrized into the OPLS formulation [19–21],

$$E = \frac{1}{2}K_1(1 + \cos\varphi) + \frac{1}{2}K_2(1 - \cos2\varphi) + \frac{1}{2}K_3(1 + \cos3\varphi) + \frac{1}{2}K_4(1 - \cos4\varphi). \quad (12)$$

The fitting results and potential parameters were compiled in the Supplemental Material [35]. The Dreiding force field was employed [26] for all-atom atomistic simulations, and the atomistic trajectories of DPDCPB molecules were collected at temperature equal to 500 K.

In the present study, the CGMD simulations were performed using the Large-scale Atomic/Molecular Massively Parallel Simulator (LAMMPS) package with GPU acceleration [36]. As depicted schematically in Fig. 1, for DPDCPB

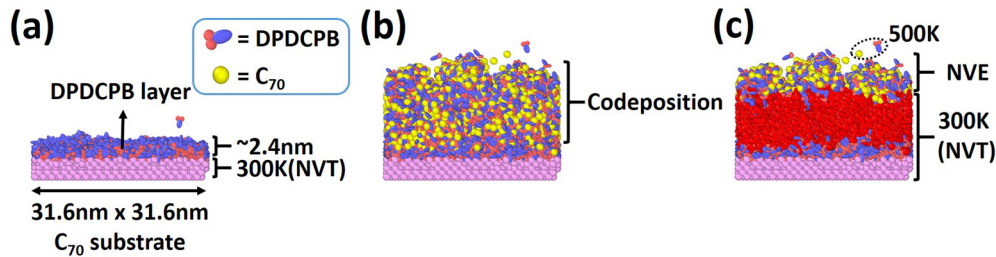


FIG. 3. Schematics of deposition simulation. (a) The pure DPDCPB layer atop the  $C_{70}$  slab for subsequent codeposition; (b) codeposition simulation of  $C_{70}$  and DPDCPB molecules on the DPDCPB layer supported by  $C_{70}$  substrate; (c) thermostats employed during the codeposition simulations.

molecules, atoms were divided into three groups: one DCPB group (atoms 7, 8, and 9) and two DP groups (atoms 1, 2, and 3; atoms 4, 5, and 6). The conformations of DPDCPB molecules during CGMD simulations were preserved by making each of the atom groups (namely the DCPB and DP groups) rigid bodies and assigning virtual atoms to anchor CG bonds.

The CGMD simulations of vacuum deposition were performed by the following procedure:

(i) Release a fixed number of  $C_{70}$  and DPDCPB molecules 3 nm above the growing film surface at randomly picked lateral locations/orientations with kinetic energies equivalent to 500 K (velocities of  $1.727 \times 10^{-3}$  and  $1.2185 \times 10^{-3}$ /fs for DPDCPB and  $C_{70}$ , respectively) for every predefined time interval  $\tau$ . Note that the velocity vectors of incoming molecules were randomly chosen with the vertical component pointing downward to ensure deposition.

(ii) Equilibrate the entire system by running CGMD simulation. Relax the newly deposited molecules under the *NVE* ensemble for 1–2 ns to allow them to dissipate their thermal energies to the underlying molecules subjected to the *NVT* ensemble with temperature controlled at 300 K [Fig. 3(c)]. After equilibration, append these newly deposited molecules to the group of molecules subjected to the *NVT* ensemble.

(iii) Repeat.

Before codeposition of DPDCPB: $C_{70}$  blends, a substrate comprising pure DPDCPB molecules had to be prepared. The DPDCPB substrate was prepared by depositing DPDCPB molecules onto a  $C_{70}$  slab in the face-centered-cubic (fcc) structure [37] (lattice parameter 1.58 nm) with a lateral dimension of  $31.6 \times 31.6 \text{ nm}^2$ . The  $C_{70}$  supporting layer was controlled at 300 K by the Nose-Hoover thermostat, while the DPDCPB molecules were assigned a kinetic energy equivalent to 500 K and were deposited onto the  $C_{70}$  supporting layer until there were approximately 3000 DPDCPB molecules deposited (roughly 2.4 nm in thickness) [Fig. 3(a)]. Note that the  $C_{70}$  supporting layer was considered to be the reservoir to absorb the thermal energy from the incoming DPDCPB molecules. After the preparation of the DPDCPB substrate, DPDCPB and  $C_{70}$  molecules were deposited together to simulate the codeposition processes. To explore the effects of DPDCPB: $C_{70}$  blending ratios on the morphologies of bulk heterojunction layers, three different deposition simulations with DPDCPB: $C_{70}$  deposition ratios 1:1, 2:1, and 3:1 were performed. Note that the deposition ratio in the present study refers to the number ratio of DPDCPB: $C_{70}$  deposited, i.e.,

the deposition ratio 3:1 refers to depositing three DPDCPB molecules and one  $C_{70}$  molecule for each deposition interval  $\tau$ . Figure 3(b) displays a snapshot from the 1:1 deposition ratio simulation. To fix the incoming flux of DPDCPB and  $C_{70}$  (i.e., the average number of both arriving DPDCPB and  $C_{70}$  molecules per unit time), the  $\tau$  values for each deposition cycle were 20, 30, and 40 ps for blending ratios 1:1, 2:1, and 3:1, respectively.

### III. RESULTS AND DISCUSSION

#### A. Morphological evolution and roughness analysis

The morphological evolution of DPDCPB: $C_{70}$  films during vacuum codeposition simulations with different blending ratios is displayed in Fig. 4. The film thicknesses for all three deposition simulations are approximately 17.25 nm, which is compatible with those from experiments [17]. The film surfaces are rough, with unfilled pits and crosslinks between nanopillars comprising DPDCPB and  $C_{70}$  molecules. From Fig. 4, it seems that increasing the amount of  $C_{70}$  leads to increasing surface roughness and unfilled pits. This trend becomes more pronounced with film growth beyond 14.75 nm. Figure 5 displays the film cross-sections of all blending ratios as film thickness reached 17.25 nm. Unfilled pits or cavities are clearly visible, and it is evident that the 1:1 film yields the largest cavity among all blending ratios investigated. Furthermore, it appears that the backbone of the surface feature primarily comprises  $C_{70}$  aggregates, which could be attributed to the strong attractive interactions between  $C_{70}$  beads (see Fig. 2). Recent all-atom molecular simulation of the deposition process of bulk heterojunction photovoltaic cells also revealed similar phenomena [38]. In the following, further quantitative analysis will be performed to examine surface roughness, density along film thickness, surface/interior composition, and coordination numbers of  $C_{70}$ . The morphological properties, including the domain percolations and specific interfacial areas, will be evaluated to provide insights into the correlations between film roughness, deposition ratios, and device performance.

Surface roughness measurements from AFM are the only morphological properties that can allow direct comparisons with CGMD deposition simulations in the present study. The surface roughness  $R_{\text{rms}}$  was computed by calculating the root-mean-square (rms) differences of the local film height across the measured region, namely the simulation cell in the present

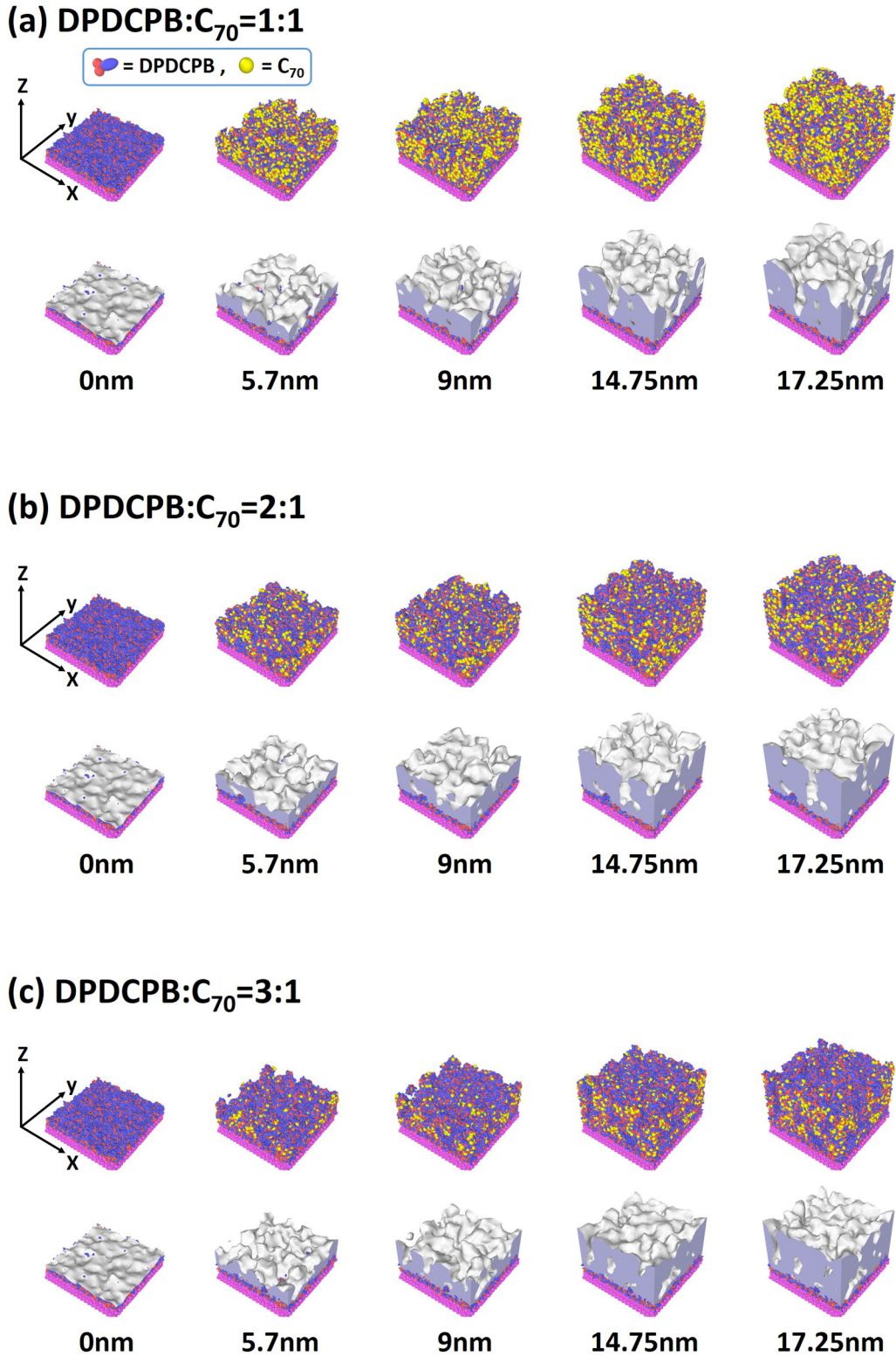


FIG. 4. Morphological evolution of the active layer during the codeposition process. Parts (a)–(c) show the morphological evolution of the DPDCPB:C<sub>70</sub> blending ratios 1:1, 2:1, and 3:1, respectively. The lower panels highlight the free surface in the growing films.

study, which is defined as

$$R_{\text{rms}} = \sqrt{\frac{1}{N_g} \sum_{i=1}^{N_g} (h_i - \bar{h})^2}, \tag{13}$$

where  $N_g$  is the number of grids in the lateral dimensions (namely, the  $X$  and  $Y$  directions) with grid size equal to  $1\text{nm}^2$ ,  $h_i$  is the height of the highest atom in each grid, and  $\bar{h}$  is the average film thickness defined as the mean of  $h_i$ . The surface roughness values as functions of film thickness for

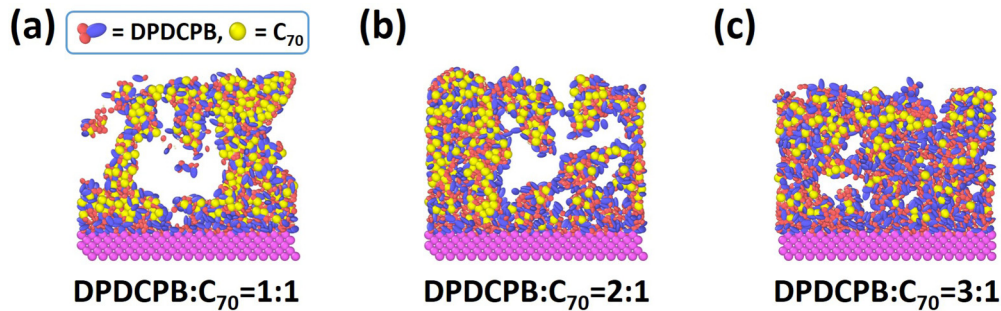


FIG. 5. The film cross-sections of DPDCPB: $C_{70}$  blending ratios (a) 1:1, (b) 2:1, and (c) 3:1.

all DPDCPB/ $C_{70}$  blending ratios are displayed in Fig. 6(a). The initial thickness and rms roughness of the DPDCPB substrate layer were 2.40 and 0.73 nm, respectively. Regardless of the deposition ratios, the surface roughness increases almost linearly with increasing film thickness until the film thickness reaches approximately 5 nm. Note that there are no significant differences in surface roughness for all deposition ratios at this stage. The surface roughening trend curtailed as films grew beyond 5 nm; in particular, for the DPDCPB: $C_{70}$  deposition ratio of 3:1, the surface roughness reaches a plateau and shows no sign of further surface roughening. Figure 6(b) displays the simulated AFM image of the surface topology by compiling the local film height across the lateral film

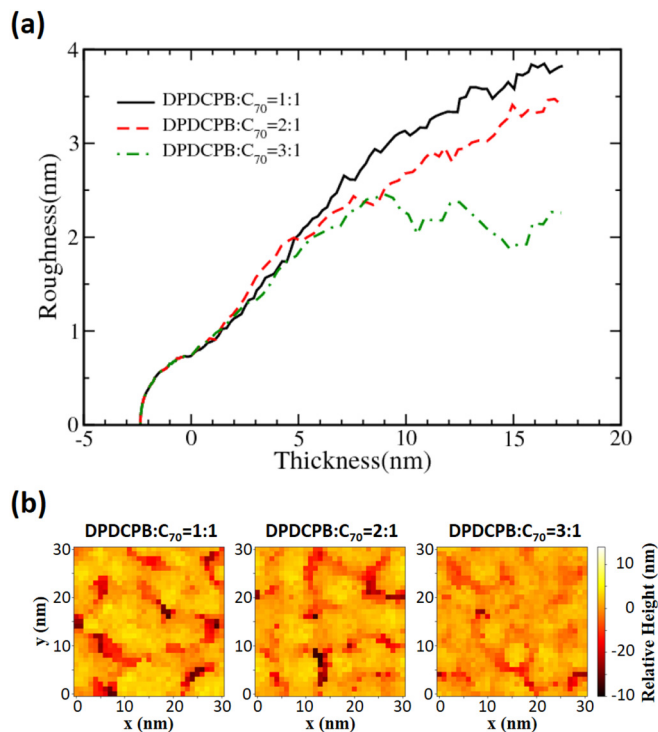


FIG. 6. (a) The surface roughness vs film thickness for different DPDCPB: $C_{70}$  blending ratios. The solid black, red dashed, and the green dot-dashed lines are the results of the blending ratio 1:1, 2:1, and 3:1, respectively. (b) The simulated AFM surface topography images of the 1:1 (left), 2:1 (middle), and 3:1 (right) ratios. The color bars showed the relative height, with the average film height set as zero. The lateral resolution of simulated AFM topography was  $1 \text{ nm}^2$ .

dimensions. Note that the 1:1 film (with high  $C_{70}$  concentration) appears to have larger grains and rougher surface than the ones with low  $C_{70}$  concentration (2:1 and 3:1). From Fig. 6, the rms surface roughness computed from our CGMD simulations is in good agreement with measurements from AFM experiments [39,40] as well as from all-atom atomistic molecular-dynamics simulations [38].

We performed fractal analysis by computing the dependency of the rms surface roughness with respect to the lateral length scale  $L$  (namely, the lateral bin sizes in computing rms surface roughness). The analysis results are displayed in Fig. 7, and two exponents, namely local exponents  $\alpha_1$  and global exponents  $\alpha_2$ , can be fitted by the power laws for each deposition ratio; see the dashed and dotted lines, respectively, in Fig. 7. The magnitudes of  $\alpha_1$  and  $\alpha_2$  are compiled in Table I. The growth mode can be viewed as diffusion-limited if  $\alpha_1 \approx 1$  [41,42]; hence, our analysis implies that the growth modes in the present study are not fully diffusion-limited, that is, there is noticeable surface diffusion of molecules involved during growth. Nevertheless, the  $\alpha_1$  magnitudes for three deposition ratios suggest that the 1:1 film (with high  $C_{70}$  concentration) is closer to the diffusion-limited mode than the 3:1 film. The small magnitudes of fitted  $\alpha_2$  in Table I also suggests negligible lateral growth [43,44]. The intersections of the fitted lines of  $\alpha_1$  and  $\alpha_2$  can be interpreted as the grain sizes [44], and the estimated grain sizes of different deposition ratios are

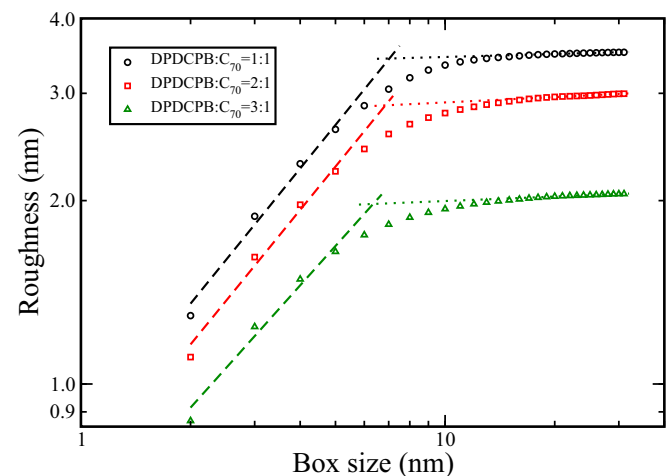


FIG. 7. Fractal analysis of the film surface with different deposition ratios. The slopes of the dashed/dotted lines are the fitted local/global exponents, respectively.

TABLE I. Local/global exponents, and grain sizes computed from fractal analysis for all deposition ratios.

DPDCPB:C <sub>70</sub>	Local exponent $\alpha_1$	Global exponent $\alpha_2$	Grain size $L_c$ (Å)
1:1	0.736975	0.0162955	70.312606
2:1	0.733446	0.0294029	68.542956
3:1	0.666713	0.0244503	63.449585

compiled in Table I. The estimated grain size of the 3:1 film is the smallest among the three deposition ratios, which is in accordance with simulated AFM images in Fig. 6(b).

### B. Molecular number density profile analysis

Molecular number density profile analysis, i.e., computing the number density of molecules along the growing direction of the film (namely the positive  $z$ -direction in Fig. 4), can provide quantitative insights into film compactness as well as film roughness. The density profile  $d(z)$  was computed by dividing the film into equally spaced bins along the  $z$ -direction, counting the number of beads within each bin, and normalizing the bin size (0.2 nm in the present study). Since DPDCPB molecules comprise multiple bonded CG beads, the central nitrogen atom was chosen to represent the location of the whole molecule in computing the number density profile  $d(z)$ . Figure 8 displays the density profiles of DPDCPB+C<sub>70</sub> for the films of different blending ratios. Note that the blue dashed lines in Fig. 8 highlight the location of the mean film thickness, which was defined as the mean value of the film height across the lateral dimension of the simulation cell for all deposition simulations. The peaks at the bottom of the film (namely,  $z$  below zero) represent the pure DPDCPB layer. For all deposition simulations, the density profiles show slight decreases until the film thickness reaches a plateau region (at the number density of roughly  $0.81/\text{nm}^3$ ) at approximately 5 nm in thickness, suggesting a gradual (but modest) decrease in film compactness, which can be correlated with the increase in surface roughness displayed in Fig. 6(a). After 5 nm, the molecular number density of the 1:1 film is noticeably

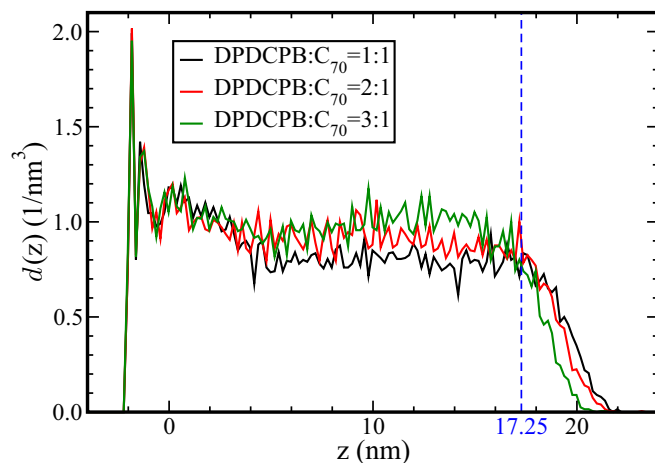


FIG. 8. The molecular number density profile  $d(z)$  analysis of different deposition ratios. The blue dashed line highlights the average thickness ( $\sim 17.25$  nm) for all blending ratios.

lower than those of the 2:1 and 3:1 films, implying that the DPDCPB/C<sub>70</sub> films with a 1:1 blending ratio are less compact relative to other blends due to the presence of cavities and unfilled pits. Note that this trend is inverted beyond the average film thickness of 17.25 nm, and that the 1:1 blending ratio yielded higher number density and longer tails (the thickness of the number density before reaching zero) relative to other deposition ratios, demonstrating that the 1:1 blending ratio yields the roughest surface.

### C. Surface/interior composition analysis

Close examination of the cross-section morphologies of DPDCPB:C<sub>70</sub> films (Fig. 5) suggests that the C<sub>70</sub> aggregated in the film interior serves as the backbone of the film structure. Two issues need to be addressed to reveal the aggregation behavior of C<sub>70</sub> in the film, as well as its implications to the overall film structures:

(i) Composition of DPDCPB/C<sub>70</sub> in both film surface/interior—the composition of C<sub>70</sub> in film surface/interior relative to the respective nominal composition for a given DPDCPB:C<sub>70</sub> blending ratio.

(ii) The coordination number analysis of C<sub>70</sub> molecules—which indicates whether C<sub>70</sub> molecules preferred being surrounded by C<sub>70</sub> molecules.

To analyze DPDCPB/C<sub>70</sub> compositions in the film surface/interior, we first split the film molecules into surface and interior molecules, and then we analyzed their respective molecular compositions. Derived from the concept of the contact number analysis [45–48], we filled the empty space in the simulation cell with small pseudoparticles. Counting the number of pseudoparticles in the clusters (aggregates of pseudoparticles) allowed us to isolate free surface and cavities by eliminating tiny packing spaces between neighboring molecules. The molecules in contact with these pseudospheres were considered to be surface molecules, whereas the rest of the molecules were assigned as interior molecules. Figures 9(a)–9(c) displayed the split film surface (upper panels) and interior (lower panels) of deposition ratios 1:1, 2:1, and 3:1. For all deposition ratios, it appears that most of the C<sub>70</sub> molecules are distributed in the film interior. Figure 10(a) displays the molecular composition of the film surface/interior at different deposition ratios. The solid and hollow bars refer to the local (i.e., the actual film surface/interior) and nominal film molecular compositions, respectively. It is evident that for all deposition ratios, the C<sub>70</sub> (DPDCPB) compositions in the film interior (surface) are noticeably higher than the nominal C<sub>70</sub> (DPDCPB) compositions, suggesting that C<sub>70</sub> (DPDCPB) molecules prefer to reside within the interior (surface) of the film. Next, we examined the C<sub>70</sub> coordination numbers in the film interior region [lower panels in Figs. 9(a)–9(c)]. In computing the C<sub>70</sub> coordination numbers, a cutoff distance of

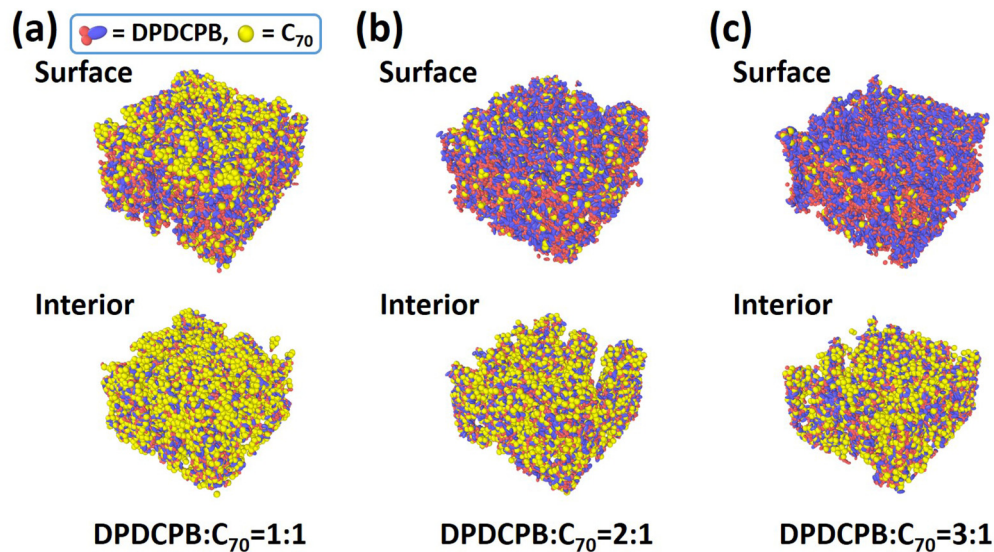


FIG. 9. Snapshots of the film surface (upper panels) and interior (lower panels) of DPDCPB:C<sub>70</sub> films with different blending ratios: (a) 1:1; (b) 2:1; (c) 3:1.

1.25 nm was specified by examining the radial distribution function (RDF) of C<sub>70</sub> molecules in the film interior: see Fig. S4 in the Supplemental Material [35]. This choice of cut-off distance would allow accommodation of all C<sub>70</sub>-C<sub>70</sub> and

C<sub>70</sub>-DCPB molecules in the first shell of the RDF (Fig. S4). The coordination fraction analysis of C<sub>70</sub> molecules under different deposition ratios is displayed in Fig. 10(b). Once again, the hollow bars refer to the nominal coordination fraction of C<sub>70</sub> with neighboring DPDCPB/C<sub>70</sub> molecules. From Fig. 10(b), it is evident that C<sub>70</sub> molecules tend to be surrounded by C<sub>70</sub> molecules regardless of deposition ratios. This indicates the formation of C<sub>70</sub> aggregates in the film interior, which can be attributed to the strong attractive interactions between C<sub>70</sub> molecules. Note that, although the potential well of the DCPB-C<sub>70</sub> pairs is slightly lower than the C<sub>70</sub>-C<sub>70</sub> pairs (see Fig. 2), the geometric confinement effects from both the highly anisotropic DCPB beads and the attached DPDCPB molecules constrain the number of DCPB beads in contact with C<sub>70</sub> molecules. As a result, C<sub>70</sub> molecules form aggregates, leading to a rough film surface with C<sub>70</sub>-rich aggregates serving as the backbone of the film.

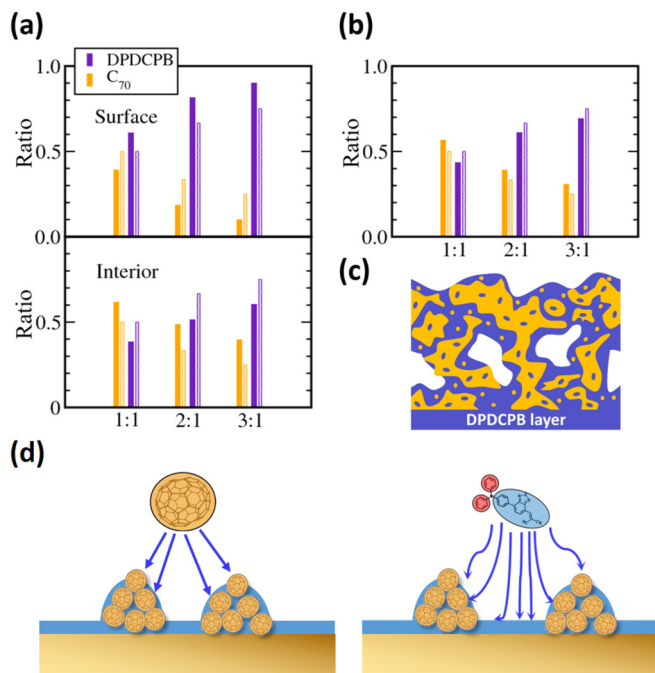


FIG. 10. (a) Molecular composition of the film surface/interior and (b) coordination number of C<sub>70</sub> molecules with DCPB and C<sub>70</sub> in the film interior at different blending ratios. Solid and hollow bars denote the local (namely, film surface/interior) and nominal molecular compositions, respectively; (c) schematic image depicting the DPDCPB:C<sub>70</sub> film microstructure. Yellow and blue domains denote C<sub>70</sub> and DPDCPB domains, respectively; (d) schematic illustration about the differences in deposition over an unfilled pit between a C<sub>70</sub> (left panel) and a DPDCPB (right panel) molecule.

According to this quantitative analysis, the detailed microstructure of DPDCPB:C<sub>70</sub> film can be depicted schematically in Fig. 10(c). Due to the strong C<sub>70</sub>-C<sub>70</sub> interaction and compact shape, C<sub>70</sub> molecules [the domains colored in yellow in Fig. 10(c)] show a strong tendency to aggregate and form the backbone of surface structures; in contrast, DPDCPB molecules tend to wrap around the C<sub>70</sub> clusters, forming core-shell-like nanostructures. The size of the “core” and the thickness of the “shell” depend on the nominal concentrations of C<sub>70</sub> and DPDCPB. If the deposition ratio of C<sub>70</sub> is high, the amount of DPDCPB molecules would not be sufficient to form a thick DPDCPB overlayer, or even to passivate C<sub>70</sub> skeletons [e.g., 1:1 film; see Fig. 9(a)]. Since the transport of holes in the active layer of small-molecule organic solar cells relies on carrier (namely, holes) hopping in the DPDCPB domains, thin or even truncated DPDCPB layers may hinder hole transport or even promote recombination. We will perform a morphological property analysis to evaluate the specific interfacial areas and domain percolations in the next subsection.

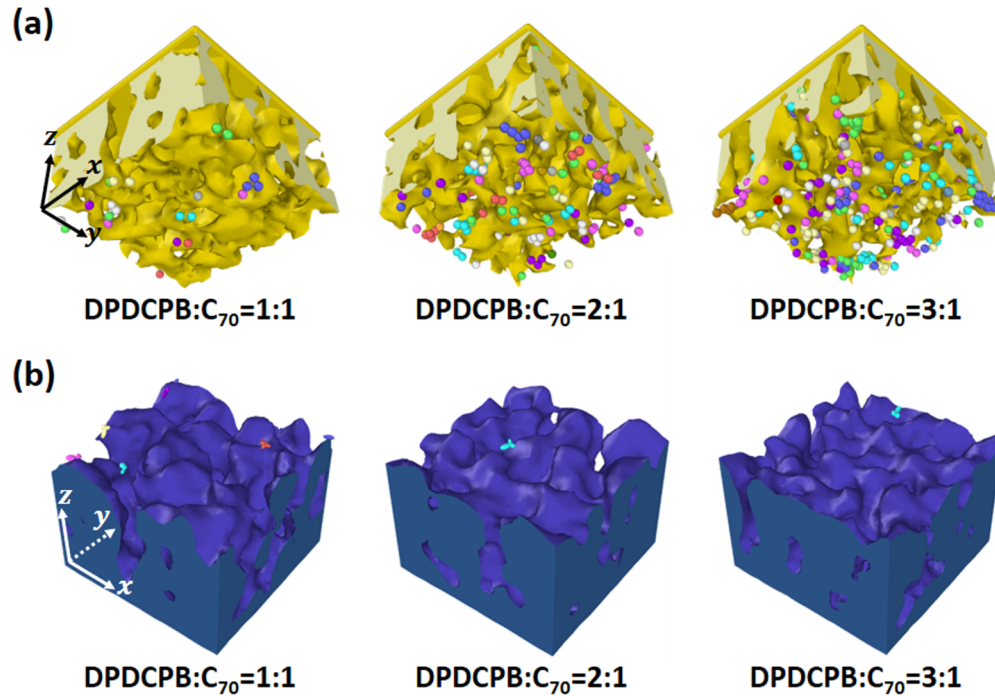


FIG. 11. (a) Percolated  $C_{70}$  domains to the pseudocathode; (b) percolated DPDCPB domains to the anode. Note that the colored ellipsoids in (a) and (b) denote isolated  $C_{70}$  /DPDCPB molecules, and molecules are colored in identical colors if they belong to the same isolated molecular clusters.

Our deposition simulations have shown that a high  $C_{70}$  deposition ratio leads to poor film quality with cavities and unfilled pits relative to other deposition ratios with lower  $C_{70}$  nominal concentrations (namely, 2:1 or 3:1). Earlier experimental and molecular simulation works also revealed that fullerene molecules tend to form a rough film surface, and the introduction of donor molecules can effectively suppress the surface roughening [38,40]. We believe that the roughening of the growing surface and the formation of cavities during deposition are closely correlated with the intermolecular attractive interactions between molecules. Imagine a growing DPDCPB: $C_{70}$  surface with a pit surrounded by surface mounds, as illustrated schematically in Fig. 10(d). According to our above-mentioned analysis, the core of these mounds is primarily comprised of  $C_{70}$  molecules. There is also a fraction of  $C_{70}$  molecules dispersed on the mound surface. Due to the strong, long-ranged, and almost isotropic (relative to other ellipsoidal particles in the system) intermolecular attractive interactions between  $C_{70}$  molecules, the incoming  $C_{70}$  molecules would have a very high probability to be attracted to the surface mounds, thereby leaving the pit unfilled and forming a cavity upon further film growth. In contrast, the interaction between DPDCPB and DPDCPB or between DPDCPB and  $C_{70}$  molecules is highly anisotropic, with a relatively shorter interaction range than the  $C_{70}$ - $C_{70}$  pairs (Fig. 2); therefore, the incoming DPDCPB molecules have a better chance to escape from attractive interactions from molecules in the mounds and deposit at the pit. Hence, the role played by DPDCPB molecules in the surface morphology is to suppress the tendency of surface roughening.

#### D. Morphological property analysis

Both donor/acceptor domain percolations and specific interfacial area are critical morphological properties that can be correlated with device performance. Herein, we analyzed the DPDCPB/ $C_{70}$  domain percolations by contact-recognition, i.e. identifying if the two ellipsoids come into contact based on their shape matrix  $\mathbf{S}$  of ellipsoids. For  $C_{70}$  domain percolation analysis, a pseudocathode was imposed by inserting a  $C_{70}$  slab at film height 17.25 nm—the average film thickness. Note that two DPDCPB molecules were considered to be connected if any ellipsoids comprised of the DPDCPB molecules (namely, DT and DCPB) were in contact with ellipsoids of the neighboring DPDCPBs. The percolated  $C_{70}$ /DPDCPB domains are displayed in Figs. 11(a) and 11(b), respectively. Note that the colored beads in Figs. 11(a) and 11(b) denote the isolated clusters of  $C_{70}$  and DPDCPB molecules, respectively. For the  $C_{70}$  molecules, most of the isolated  $C_{70}$  clusters are distributed in the region adjacent to the DPDCPB substrate, and there are more isolated  $C_{70}$  clusters in the 3:1 film than in the 1:1 film. The specific interfacial area (the amount of interfacial area per unit volume) and DPDCPB/ $C_{70}$  percolation ratios are compiled in Table II. Note that the 1:1 film has the highest specific interfacial area and domain percolations relative to the 2:1 and 3:1 films, despite its poor film quality. Both the specific interfacial area and the domain percolation analysis suggest that the 1:1 film should yield the best performance, which is not in agreement with experimental evaluations (the 2:1 film gave the best performance [17]). The disagreement may originate from the quality or the strength of domain percolations, and it will be examined further.

TABLE II. The morphological properties of deposited films.

DPDCPB:C <sub>70</sub>	Specific interfacial area (1/nm)	DPDCPB percolation (%)	C <sub>70</sub> percolation (%)
1:1	1.10583	~100	99.67
2:1	1.09055	~100	97.49
3:1	0.9243	~100	92.42

Figures 12(a) and 12(b) display the DPDCPB (a) and C<sub>70</sub> (b) domain percolations of different deposition ratios as a function of the allowed hole/electron hopping distance used to determine the connectivity of the DPDCPB/C<sub>70</sub> phase. Note that the hopping distance of DPDCPB or C<sub>70</sub> was defined as the distance between neighboring nitrogen atoms or the center of mass of C<sub>70</sub>, respectively. Hence, Fig. 12 implies an abundance of DPDCPB/C<sub>70</sub> connecting pathways over different predefined nitrogen-nitrogen/C<sub>70</sub>-C<sub>70</sub> separation. From Fig. 12(a), a hopping distance of 1 nm [highlighted by the blue dashed line in Fig. 12(a)] can connect to ~90% and ~75% of the DPDCPB domains for the 3:1 and 2:1 films; in contrast, only ~15% of the DPDCPB domains are connected for the 1:1 film with identical hopping distance. Note that ~90% of the

DPDCPB domains of the 1:1 film can only be connected when the hopping distance is extended to 1.2 nm. The morphologies of the percolated DPDCPB domains with hopping distance set to 1 nm are displayed in the insets of Fig. 12(a), and it is clear that for the 1:1 film, only the bottom (close to the anode) part of the DPDCPB domains is percolated, whereas almost all of the DPDCPB domains are percolated for the 3:1 and 2:1 films. These suggest that the transport pathways of the 1:1 film in the middle/top parts of the bulk heterojunction rely primarily on longer hopping distance relative to the 3:1 and 2:1 films, or there are fewer available hole hopping pathways between DPDCPB molecules in the 1:1 film than in the 3:1 and 2:1 films, which is also evidenced by the higher magnitudes of RDFs between DCPB pairs in the 3:1 and 2:1 films than in the 1:1 film (Fig. S4). Hence, despite the fact that the estimated DPDCPB percolations in all three deposition ratios are close to 100% based on contact recognition, the percolation “quality” of the DPDCPB domain in the 2:1 and 3:1 films is better than that of the 1:1 film because of more available hopping pathways and shorter hopping distance for the holes in the 2:1 and 3:1 films than in the 1:1 film. Therefore, the hole mobility of both the 2:1 and 3:1 films should be expected to be higher than that of the 1:1 film.

For the C<sub>70</sub> domains, from Fig. 12(b) we can see that in contrast to DPDCPB domains, the C<sub>70</sub> domain percolation ratios rise rapidly beyond 1.1 nm. A hopping distance of 1.2 nm [highlighted by the blue dashed line in Fig. 12(b)] can connect to 80%, 94%, and ~100% of the C<sub>70</sub> domains in the 3:1, 2:1, and 1:1 films, respectively. From the insets of Fig. 12(b) it is also evident that the 3:1 film has more isolated C<sub>70</sub> clusters (the colored beads in the insets) than the 1:1 and 2:1 films, despite the fact that most of the C<sub>70</sub> domains are percolated in all deposition ratios. Hence, both Table II and Fig. 12(b) suggest that the 1:1 film gives better C<sub>70</sub> domain percolations as well as percolation quality than the 2:1 and 3:1 films, implying that the 1:1 film should yield the best electron transport to the cathode over the 2:1 and 3:1 films.

The DPDCPB/C<sub>70</sub> domain percolation quality analysis can therefore resolve the disagreements in the optimal blending ratio between morphological property analysis predictions (suggesting that 1:1 should be the optimal ratio) and actual experimental results (2:1). In the 1:1 film, the DPDCPB domain can be viewed as “weakly connected” relative to the 2:1 and 3:1 films due to its longer hole hopping distance and fewer transport pathways. As a result, the hole transport in the 1:1 film could be noticeably inferior to those in the 2:1 and 3:1 films. Despite the fact that the C<sub>70</sub> domain in the 1:1 film is better connected than the other two films, there might not be a huge difference in electron collection at the pseudocathode. On the other hand, the DPDCPB (C<sub>70</sub>) domain connectivity in the 2:1 film is only slightly lower than that in the 3:1 (1:1) films, providing the most balanced charge carrier transport,

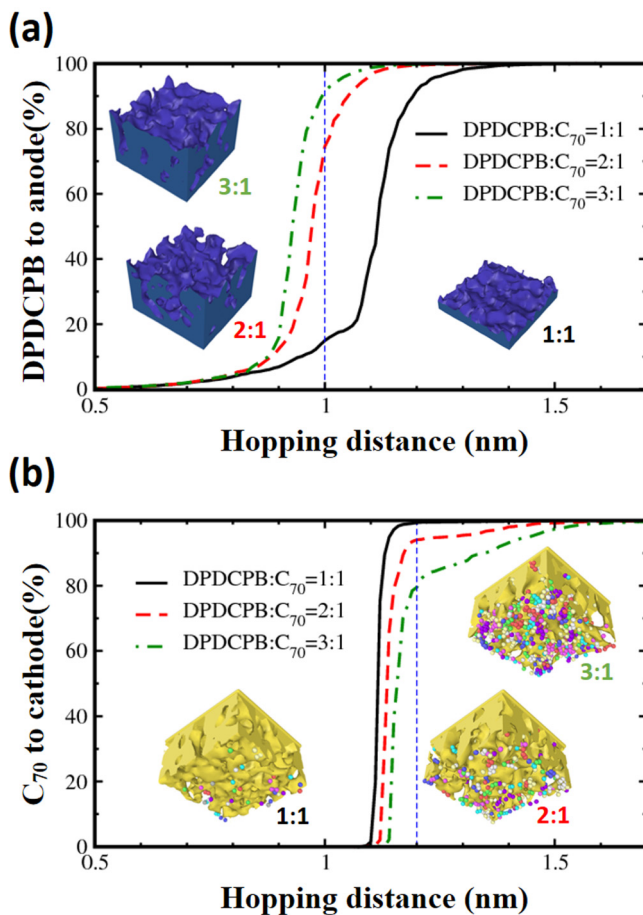


FIG. 12. The DPDCPB (a) and C<sub>70</sub> (b) domain percolations of different deposition ratios as a function of the allowed hole/electron hopping distance used to determine the connectivity of the DPDCPB/C<sub>70</sub> phase. The insets in (a) [(b)] display the percolated DPDCPB/C<sub>70</sub> domains with 1.0 nm (1.2 nm) hopping distance [highlighted by the blue dashed lines in (a) and (b)], respectively.

and this might be the primary reason why the 2:1 film yields the best performance experimentally. Nevertheless, further multiscale calculations incorporating mesoscale charge carrier transport simulations such as kinetic Monte Carlo based on the Marcus theory could potentially provide direct links between morphologies and charge transport [49].

#### IV. CONCLUSIONS

In the present paper, we investigated the morphological evolution of the DPDCPB:C<sub>70</sub> small-molecule organic solar cells during vacuum deposition processes by performing a series of CGMD simulations. A significant reduction in the total system degrees of freedom by coarsening C<sub>70</sub> and DPDCPB molecules into ellipsoids and bonded ellipsoids allowed us to simulate film deposition processes with system sizes compatible with experiments. This CG scheme can be readily extended to other small-molecule-based organic electronic devices, such as OLEDs. Our CGMD simulations indicate that the DPDCPB:C<sub>70</sub> deposition ratio noticeably impacts film morphologies. Films grown with a high C<sub>70</sub> deposition ratio contain more visible defects, such as unfilled pits, cavities, and larger grains than those grown with low C<sub>70</sub> deposition ratios, which was confirmed quantitatively by surface roughness analysis and fractal analysis. The surface roughness from deposition simulations is in good agreement with AFM measurements. Subsequent analysis suggests that C<sub>70</sub> molecules

tend to aggregate, forming the backbone of surface structures, whereas DPDCPB molecules passivate the C<sub>70</sub> backbone, forming core-shell-like structures. Despite the rough surface and cavities, surprisingly, morphological property analysis suggested that both DPDCPB and C<sub>70</sub> domains retain high percolation ratios. Nevertheless, analysis of DPDCPB domain percolation quality suggested that the hole transport pathways in the 1:1 film are “weakly connected” due to the longer hopping distance and fewer transport pathways relative to both the 2:1 and 1:1 films. This suggests that in addition to specific interfacial area and donor/acceptor domain percolation ratios, the strength of the percolation also needs to be examined. The present paper, therefore, demonstrated that the bonded ellipsoid CG scheme can be utilized to investigate the morphological evolution of small-molecule thin films during vacuum deposition processes with system sizes compatible with experiments, in combination with molecular details, thereby providing valuable insights into the process-structure-property correlations of organic electronic materials.

#### ACKNOWLEDGMENTS

The authors gratefully acknowledge the financial support from the Academia Sinica Sustainability Science Project, Grant No. AS-SS-109-05, and the Ministry of Science and Technology, Taiwan, Grant No. MOST 105-2112-M-001-009-MY3. We also thank the National Center for High-performance Computing, Taiwan for computational support.

- 
- [1] T. Ameri, G. Dennler, C. Lungenschmied, and C. J. Brabec, *Energy Environ. Sci.* **2**, 347 (2009).
  - [2] K. M. Coakley and M. D. McGehee, *Chem. Mater.* **16**, 4533 (2004).
  - [3] Y. J. Cheng, S. H. Yang, and C. S. Hsu, *Chem. Rev.* **109**, 5868 (2009).
  - [4] C. D. Dimitrakopoulos and P. R. L. Malenfant, *Adv. Mater.* **14**, 99 (2002).
  - [5] H. Hoppe and N. S. Sariciftci, *J. Mater. Res.* **19**, 1924 (2004).
  - [6] H. Spanggaard and F. C. Krebs, *Solar Energy Mater. Solar Cells* **83**, 125 (2004).
  - [7] B. C. Thompson and J. M. J. Frechet, *Angew. Chem. Int. Ed.* **47**, 58 (2008).
  - [8] S. Gunes, H. Neugebauer, and N. S. Sariciftci, *Chem. Rev.* **107**, 1324 (2007).
  - [9] L. Lu, W. Chen, T. Xu, and L. Yu, *Nat. Commun.* **6**, 7327 (2015).
  - [10] L. Lu, M. A. Kelly, W. You, and L. Yu, *Nat. Photon.* **9**, 491 (2015).
  - [11] G. Yu and A. J. Heeger, *J. Appl. Phys.* **78**, 4510 (1995).
  - [12] J. J. M. Halls, C. A. Walsh, N. C. Greenham, E. A. Marseglia, R. H. Friend, S. C. Moratti, and A. B. Holmes, *Nature (London)* **376**, 498 (1995).
  - [13] H. Hoppe and N. S. Sariciftci, *J. Mater. Chem.* **16**, 45 (2006).
  - [14] X. Yang and J. Loos, *Macromolecules* **40**, 1353 (2007).
  - [15] C. K. Lee, C. W. Pao, and C. W. Chu, *Energy Environ. Sci.* **4**, 4124 (2011).
  - [16] C. K. Lee and C. W. Pao, *ACS Appl. Mater. Interfaces* **8**, 20691 (2016).
  - [17] Y. H. Chen, L. Y. Lin, C. W. Lu, F. Lin, Z. Y. Huang, H. W. Lin, P. H. Wang, Y. H. Liu, K. T. Wong, J. Wen, D. J. Miller, and S. B. Darling, *J. Am. Chem. Soc.* **134**, 13616 (2012).
  - [18] J. G. Gay and B. J. Berne, *J. Chem. Phys.* **74**, 3316 (1981).
  - [19] W. L. Jorgensen and T. R. Julian, *J. Am. Chem. Soc.* **110**, 1657 (1988).
  - [20] W. L. Jorgensen, D. S. Maxwell, and T. R. Julian, *J. Am. Chem. Soc.* **118**, 11225 (1996).
  - [21] E. K. Watkins and W. L. Jorgensen, *J. Phys. Chem. A* **105**, 4118 (2001).
  - [22] J. W. Perram, J. Rasmussen, E. Praestgaard, and J. L. Lebowitz, *Phys. Rev. E* **54**, 6565 (1996).
  - [23] R. Berardi, C. Fava, and C. Zannoni, *Chem. Phys. Lett.* **297**, 8 (1998).
  - [24] R. Everaers and M. R. Ejtehadi, *Phys. Rev. E* **67**, 041710 (2003).
  - [25] M. P. Allen and G. Germano, *Mol. Phys.* **104**, 3225 (2006).
  - [26] S. L. Mayo, B. D. Olafson, and W. A. Goddard, *J. Phys. Chem.* **94**, 8897 (1990).
  - [27] N. Hansen, *Studies in Fuzziness and Soft Computing* (Springer, Berlin, 2006), Vol. 192, p. 75.
  - [28] N. Hansen and A. Ostermeier, *Evolutionary Comput.* **9**, 159 (2001).
  - [29] N. Hansen and S. Kern, in *Proceedings of the 8th International Conference on Parallel Problem Solving from Nature, Birmingham, UK*, edited by X. Yao (Springer, Birmingham, UK, 2004), Vol. 3242, pp. 282–291.
  - [30] N. Hansen, S. D. Muller, and P. Koumoutsakos, *Evolutionary Comput.* **11**, 1 (2003).

- [31] N. Hansen, R. Ros, N. Mauny, M. Schoenauer, and A. Auger, *Appl. Soft Comput.* **11**, 5755 (2011).
- [32] C. Igel, N. Hansen, and S. Roth, *Evolutionary Comput.* **15**, 1 (2007).
- [33] M. Jebalia, A. Auger, and N. Hansen, *Algorithmica* **59**, 425 (2011).
- [34] T. Suttrop, N. Hansen, and C. Igel, *Machine Learning* **75**, 167 (2009).
- [35] See Supplemental Material at <http://link.aps.org/supplemental/10.1103/PhysRevMaterials.4.095601> for the fitting results of an intramolecular CG force field including CG bonds (Fig. S1), angles (Fig. S2), and dihedrals (Fig. S3) in the coarse-grained DPDCPD molecule; the related numerical data are compiled in Table S1. Also, the numerical data of Gay-Berne potential fitted with the PES of the all-atom atomistic simulation in Fig. 2 were collected in Table S2. Figure S4 shows the radial distribution function of C<sub>70</sub> molecule and DCPB-DCPB beads.
- [36] <http://lammps.sandia.gov/>.
- [37] A. P. Isakina, A. I. Prokhvatilov, M. A. Strzhemechny, and K. A. Yagotintsev, *Low Temp. Phys.* **27**, 1037 (2001).
- [38] T. Lee, A. Sanzogni, N. Zhangzhou, P. L. Burn, and A. E. Mark, *ACS Appl. Mater. Interfaces* **10**, 32413 (2018).
- [39] O. L. Griffith, X. Liu, J. A. Amonoo, P. I. Djurovich, M. E. Thompson, P. F. Green, and S. R. Forrest, *Phys. Rev. B* **92**, 085404 (2015).
- [40] S. Nunomura, X. Z. Che, and S. R. Forrest, *Adv. Mater.* **26**, 7555 (2014).
- [41] A. L. Barabási and H. E. Stanley, *Fractal Concepts in Surface Growth* (Cambridge University Press, Cambridge, England, 1995).
- [42] D. E. Wolf and J. Villain, *Europhys. Lett.* **13**, 389 (1990).
- [43] S. F. Edwards and D. R. Wilkinson, *Proc. R. Soc. London A* **381**, 17 (1982).
- [44] T. J. Oliveira and F. D. A. Aarão Reis, *J. Appl. Phys.* **101**, 063507 (2007).
- [45] T. Aste, M. Saadatfar, and T. J. Senden, *Phys. Rev. E* **71**, 061302 (2005).
- [46] J. D. Bernal and J. Mason, *Nature (London)* **188**, 910 (1960).
- [47] G. W. Delaney and P. W. Cleary, *Europhys. Lett.* **89**, 34002 (2010).
- [48] L. E. Silbert, D. Ertas, G. S. Grest, T. C. Halsey, and D. Levine, *Phys. Rev. E* **65**, 031304 (2002).
- [49] V. Rühle, A. Lukyanov, F. May, M. Schrader, T. Vehoff, J. Kirkpatrick, B. Baumeier, and D. Andrienko, *J. Chem. Theory Comp.* **7**, 3335 (2011).